Lawrence Berkeley National Laboratory

Lawrence Berkeley National Laboratory

Title
Surface complexation of Pb(II) by hexagonal birnessite nanoparticles

Permalink
https://escholarship.org/uc/item/6wv3d9xx

Author
Kwon, K.

Publication Date
2010-11-01

Peer reviewed

Surface complexation of Pb(II) by hexagonal birnessite nanoparticles

Kideok D. Kwon[1]*, Keith Refson[2], and Garrison Sposito[1]

[1]Geochemistry Department, Earth Sciences Division, Lawrence Berkeley National Laboratory,

Berkeley, CA 94720

[2]STFC Rutherford Appleton Laboratory, Didcot, Oxfordshire OX11 0QX, United Kingdom

*Corresponding author: kkwon@lbl.gov

Abstract

Natural hexagonal birnessite is a poorly-crystalline layer type Mn(IV) oxide precipitated by bacteria and fungi which has a particularly high adsorption affinity for Pb(II). X-ray spectroscopic studies have shown that Pb(II) forms strong inner-sphere surface complexes mainly at two sites on hexagonal birnessite nanoparticles: triple corner-sharing (TCS) complexes on Mn(IV) vacancies in the interlayers and double edge-sharing (DES) complexes on lateral edge surfaces. Although the TCS surface complex has been well characterized by spectroscopy, some important questions remain about the structure and stability of the complexes occurring on the edge surfaces. First-principles simulation techniques such as density functional theory (DFT) offer a useful way to address these questions by providing complementary information that is difficult to obtain by spectroscopy. Following this computational approach, we used spin-polarized DFT to perform total-energy-minimization geometry optimizations of several possible Pb(II) surface complexes on model birnessite nanoparticles similar to those that have been studied experimentally. We first validated our DFT calculations by geometry optimizations of (1) the Pb-Mn oxyhydroxide mineral, quenselite ($PbMnO_2OH$), and (2) the TCS surface complex, finding good agreement with experimental structural data while uncovering new information about bonding and stability. Our geometry optimizations of several protonated variants of the DES surface complex led us to conclude that the observed edge-surface species is very likely to be this complex if the singly-coordinated terminal O that binds to Pb(II) is protonated. Our geometry optimizations also revealed that an unhydrated double corner-sharing (DCS) species that has been proposed as an alternative to the DES complex is intrinsically unstable on nanoparticle edge surfaces, but could become stabilized if the local coordination environment is

well-hydrated. A significant similarity exists in the structural parameters for the TCS complex

and those for a DCS edge-surface complex that is protonated in the same manner as the optimal

DES complex, which could complicate detecting the DCS complex in X-ray absorption spectra.

1. INTRODUCTION

Hexagonal birnessite is a layer type Mn(IV) oxide composed of randomly-stacked, edge-sharing MnO_6 sheets having hexagonal symmetry (Villalobos et al., 2003, 2006; Tebo et al., 2004; Saratovsky et al., 2006). In nature, birnessite is produced by bacteria and fungi, yielding a poorly-crystalline mineral with a strong scavenging affinity for the priority metal pollutant, Pb (Wilson et al., 2001; Dong et al., 2003; Tebo et al., 2004; Hochella et al., 2005; Beak et al., 2008). This high affinity has been attributed to significant negative structural charge arising from cation vacancy defects and to nanoparticle size, leading to significant surface area at lateral edges (Villalobos et al., 2005; Takahashi et al., 2007).

The Pb(II) species adsorbed on Mn(IV) vacancies in hexagonal birnessite has been found by extended X-ray absorption fine structure (EXAFS) spectroscopy to be an inner-sphere surface complex involving Pb(II) bonded to the three surface O that surround a vacancy (O_{II}) and are doubly-coordinated to Mn(IV). This triple corner-sharing (TCS) surface complex (Fig. 1) has a characteristic Pb-nearest-Mn distance [d(Pb-Mn$_{1st}$)] of 3.74 ± 0.05 Å (Matocha et al., 2001; Morin et al., 2001; Villalobos et al., 2005; Takahashi et al., 2007). At high Pb loading, another interlayer adsorbed species, a triple edge-sharing (TES) surface complex (Fig. 1b), has been identified, wherein Pb(II) binds to two O_{II} and the one surface O (O_{III}) that is triply-coordinated to Mn near the tridentate cavity created by three edge-sharing Mn octahedra (Drits et al., 2002; Lanson et al., 2002; Manceau et al., 2002). The Pb-TES variant with Pb(II) positioned near the vacancy (Lanson et al., 2002; Grangeon et al., 2008) is regarded as more stable than the corresponding alternative surface complex with Pb(II) bonded to three O_{III}, which is similar to the local Pb(II) coordination environment in the Pb-Mn oxyhydroxide mineral, quenselite

4

[PbMnO$_2$OH (Rouse, 1971)]. In quenselite, Pb is bonded to three interlayer OH and three mineral surface O surrounding the tridentate cavity formed by edge-sharing Mn(III)O$_6$, with the unit PbO(OH)$_3$ forming zigzag chains parallel to the *a* direction between the Mn(III) octahedral sheets (Fig. 2). Thus far, however, EXAFS spectral analysis has not been able to resolve the Pb-TES structural parameters from those of the Pb-TCS complex (Manceau et al., 2002).

At the lateral edges of hexagonal birnessite, two types of Pb(II) surface complex are possible (Fig. 3): double corner-sharing (Pb-DCS) and double edge-sharing (Pb-DES). Neither Pb-DCS nor Pb-DES has been detected in well-crystallized, chemically-synthesized hexagonal birnessite. Manceau et al. (2002) reported Pb-TES instead, a finding later attributed by Takahashi et al. (2007) to the rather small surface area on lateral edges relative to that in the interlayers for well-crystallized birnessite varieties. On the other hand, Morin et al. (2001) reported a Pb(II) species adsorbed at the edges of *c*-disordered H$^+$ birnessite, a chemically-synthesized analog of the biogenic mineral, assigning it as Pb-DES with a characteristic d(Pb-Mn$_{1st}$) of 3.31 ± 0.04 Å. Villalobos et al. (2005) found spectral evidence for a Pb(II) species adsorbed at the lateral edges of δ-MnO$_2$, another chemically-synthesized birnessite analog, assigning it to Pb-DCS with a characteristic d(Pb-Mn$_{1st}$) of 3.53 ± 0.06 Å. Although this conclusion was supported by Xu et al. (2006) and Boonfueng et al. (2006) in their studies of Pb(II) adsorbed on poorly-crystalline birnessites, Takahashi et al. (2007) concluded on the basis of a systematic EXAFS study that the Pb-DCS assignment made by Villalobos et al. (2005) should have been Pb-DES instead with a characteristic d(Pb-Mn$_{1st}$) of 3.23 – 3.24 Å.

In this paper, we address the issue of Pb(II) adsorbed on edge-surface sites of hexagonal birnessite nanoparticles using geometry optimizations based on total energy minimization in

density functional theory [DFT, Payne et al. (1992)]. Our principal objective is to examine whether Pb-DES is the only stable surface complex that can occur on the lateral edges of these nanoparticles. First-principles techniques such as DFT can be applied to reduce ambiguities and guide the interpretation of EXAFS spectra by providing complementary electronic structure and bonding information about metals adsorbed on mineral surfaces (Zhang et al., 2006; Sherman et al., 2008; Hattori et al., 2009; Mason et al., 2009; Kwon et al., 2009). In particular, spin-polarized DFT (i.e., electron densities are calculated separately for spin-up and spin-down electrons) accurately predicts crystal structures and electronic properties of Mn oxides (Singh, 1997; Mishra and Ceder, 1999; Pask et al., 2001), including birnessite (Kwon et al., 2009). Moreover, advances in massively-parallel computing platforms as well as in theory have now facilitated the study of structural models that are directly relevant to natural nanoparticles (Marzari, 2006; Barnard, 2009).

This paper is organized as follows. To validate our DFT approach, we first geometry-optimized the structures of both quenselite ($PbMnO_2OH$), which has been used as a model to guide the interpretation of EXAFS spectra of Pb(II) adsorbed on birnessite (Manceau et al., 2002; Takahashi et al., 2007), and the well-characterized surface species, Pb-TCS. Then we examined Pb-TES, Pb-DES, and Pb-DCS as to whether they are stable surface complexes on birnessite nanoparticles. Our geometry optimizations included the effects of Pb(II) hydration and adsorption site protonation, characteristics which are not directly susceptible to EXAFS spectral analysis, to provide new complementary insights as to the relative stability and spectroscopic detectability or discernibility of Pb(II) surface complexes on hexagonal birnessite nanoparticles.

2. COMPUTATIONAL DETAILS

2.1. Spin-polarized planewave DFT

Our geometry optimizations were performed with the CASTEP code (Clark et al., 2005), which implements DFT in a plane-wave basis set to represent wavefunctions and uses ultrasoft pseudopotentials (Vanderbilt, 1990) to replace the strong coulomb potentials between atomic nuclei and core electrons with weak effective potentials, treating the core electrons within the usual Koelling-Harmon scalar relativistic scheme. The reference electronic configurations for the pseudopotentials were Mn ($3s^2 3p^6 3d^5 4s^2$), O ($2s^2 2p^4$), Pb ($3d^{10} 4s^2 4p^2$), and H ($1s^1$), with core radii 2.3 a_0 for Mn, 1.3 a_0 for O, 3.06 a_0 for Pb, and 0.8 a_0 for H ($a_0 = 0.52918$ Å is the Bohr radius). All calculations were performed under the generalized gradient approximation [PBE-GGA, Perdew et al. (1996)] with spin polarization and periodic boundary conditions, as discussed in detail by Kwon et al. (2009), which should be consulted for additional information about our DFT methodology as applied to hexagonal birnessite.

Because the magnetic ordering of quenselite ($PbMnO_2OH$) has not been established experimentally, we examined a non-magnetic (NM) structure for this mineral along with ferromagnetic (FM) and antiferromagnetic (AFM) ordering among the Mn spin moments. We included two types of AFM ordering: AFM2 and AFM3, which Singh (1997) has studied in $LiMnO_2$ (see Supporting Information EA-1). Although calculations were initiated for each of the spin arrangements with the electronic and spin degrees of freedom unconstrained, the initial spin configuration was always found to be preserved throughout electronic and structural relaxation. The AFM3 quenselite had a lower total energy than the NM, FM, and AFM2 by 1,050, 100, and 60 meV per formula unit, respectively, which is consistent with what Singh (1997) reported for

LiMnO$_2$. Therefore, AFM for quenselite refers to AFM3. As will be discussed below, structural parameters alone cannot be used to ascertain whether quenselite actually is in an AFM state at ambient temperature, but a spin polarization ordering such as AFM is required in order to obtain an accurate molecular structure that includes Jahn-Teller distortion. The AFM ordering was examined also for a model hexagonal birnessite nanodisk bearing Pb(II) surface complexes (Pb-TCS and Pb-DES). We found a slightly higher (by 10 to 90 meV) total energy for AFM than FM, although without noticeable structural differences; thus FM ordering was chosen for all geometry optimizations involving Pb(II) adsorbed on birnessite.

2.2. Model structures

The X-ray crystallographic data of Rouse (1971) were used to create an initial structure for quenselite after adding H to protonate interlayer O (Fig. 2). For the surface complexes of Pb(II), a nanodisk model [i.e., a discoid sheet of edge-sharing Mn octahedra approximately 1.0 or 1.5 nm in diameter (7 or 19 Mn(IV)O$_6$ octahedra)] was created using the structure of a model vacancy-free hexagonal Mn(IV)O$_2$ birnessite, based on atomic coordinates for the well-crystallized birnessite (Gaillot et al., 2003) whose structural formula is K$^+_{0.231}$Mn(III)$_{0.077}$[Mn(IV)$_{0.885}\square_{0.115}$]O$_2\cdot$0.60H$_2$O, where $\square$ represents a Mn(IV) vacancy.

Interlayer cations such as K$^+$ and Mn(III) which may be important during Pb(II) adsorption are missing in our model birnessite nanoparticles. The two nanoparticle diameters we considered are smaller than the 3- to 6-nm coherent scattering domain in the *a-b* plane that has been deduced from X-ray diffraction data for biogenic and chemically-synthesized hexagonal birnessites (Villalobos et al., 2006; Grangeon et al., 2008; Lanson et al., 2008) because they represent a compromise between realistic particle size and computational cost, allowing to investigate details

of Pb(II) surface complex bonding features. Bonds dangling from Mn-O at nanoparticle edges were charge-balanced with H or H_2 (Banerjee and Nesbitt, 1999), thus becoming the surface functional groups $\equiv$Mn-OH or $\equiv$Mn-OH$_2$ (nanoparticle chemical formulas $Mn_7O_{24}H_{20}$ or $Mn_{19}O_{54}H_{32}$). For the Pb-TCS and Pb-TES surface complexes, only the 1.5-nm nanodisk model was used in order to avoid interactions between adsorbed Pb(II) and neighboring terminal OH or OH_2.

The number of hydrating water molecules of Pb surface complexes is challenging to determine directly by experiments, but octahedral coordination including bonded surface O and hydrating H_2O is reasonable (Takahashi et al. 2007). We found that, although the presence or absence of hydrating H_2O significantly affects the characteristic Pb-Mn$_{1st}$ distances of Pb complexes, hydration numbers of Pb-TCS between three and five (i.e., coordination numbers between six and nine) caused only minor changes in these distances (< 0.01 Å). For the Pb-TCS surface complex, one Mn at the center of the vacancy-free nanodisk model was removed and one Pb(II) coordinated with three H_2O was then placed above the vacancy site so as to form bonds between Pb and the three doubly-coordinated surface O (O_{II}) around the site. On the other side of the vacancy, one Pb(II) hydrated with three H_2O was placed in the Pb-TES configuration, the overall arrangement along an axis through the vacancy thus being $Pb(H_2O)_3$-□-$Pb(H_2O)_3$ (or

TCS-□-TES, where □ represents a Mn(IV) vacancy), as suggested by the X-ray diffraction study of Lanson et al. (2002). For the Pb-DCS surface complex, Pb(II) was placed so as to bond with two singly-coordinated O (O_I) and four hydrating H_2O. For the Pb-DES complex, Pb(II) was given an additional bond with one doubly-coordinated O (O_{II}) or one triply-coordinated O (O_{III})

9

along with three to four hydrating H_2O. To examine the effects on structural parameters from protonating the surface O to which Pb(II) binds, variants of the Pb-DES and Pb-DCS complexes with protonated O_I and O_{II} were geometry optimized (Fig. 3).

2.3. Geometry optimizations

The planewave basis set was expanded to 500 eV cut-off energy for all calculations except for those in which simulation cell size for Pb complexes was examined. For $PbMnO_2OH$ (quenselite), a 5 x 5 x 3 k-point grid (or equivalent for its AFM supercells) for the first Brillouin zone (Monkhorst and Pack, 1976) was used, achieving a high convergence in atomic forces < 0.001 eV/ Å. For isolated Pb-surface complexes of a MnO_2 nanoparticle, one k-point at (0.0, 0.0, 0.0) was chosen in the geometry optimization without imposing symmetry. For Pb(II) surface complexes, a sufficiently large simulation cell is required to minimize undesired interactions between a surface complex and its images in neighboring periodic cells. A larger cell requires more computation time, but insufficient cell size can result in significant errors in the total energy and the force and, therefore, inaccurate structures. The optimal simulation cell size was determined by comparison of atomic forces for cell dimensions up to 40 Å x 40 Å x 40 Å as calculated with a cut-off energy of 360 eV (force tolerance in this self-consistent total energy calculation = 0.001 eV/ Å) and without total energy correction for a fixed basis-set size. A 20 Å x 20 Å x 16 Å cell and a 26 Å x 26 Å x 20 Å cell were chosen for DCS/DES complexes (1-nm nanoparticle) and TCS/TES complexes (1.5-nm nanoparticle), respectively, with both achieving an atomic force convergence < 0.03 eV/ Å with a 360 eV cut-off energy and interatomic distances between neighboring periodic cells > 11 Å. The choice of cell sizes is supported by no detectable band dispersion in the band structure of Pb-DCS calculated with 6 k-points.

Geometry optimizations were performed using the BFGS procedure (Pfrommer et al., 1997). The residual force and the root-mean-square stress on the geometry-optimized quenselite structure were below 0.005 eV/Å and 0.005 GPa, respectively. In optimizing the Pb-surface complexes, we did not seek absolute energy minima for the complexes at 0 K because the purpose of our calculations is to examine whether the Pb(II) surface complexes suggested by spectroscopy are stable under geometry optimization. In an effort to represent the structural parameters of a thermally-disordered complex, we geometry-optimized two to four different initial H_2O configurations in each complex while maintaining the same coordination number for Pb to determine average structural parameters and their standard deviations. The maximum force tolerance was 0.03 eV/Å (a higher tolerance was not computationally feasible). Geometry optimization for Pb-DES with a smaller force tolerance (0.006 eV/Å) produced only slight changes in the interatomic distances within the standard deviations of the average structural parameters.

3. RESULTS AND DISCUSSION

3.1. Quenselite structure

Table 1 shows that inclusion of spin polarization is essential in order to obtain an accurate quenselite structure by DFT geometry optimization (compare NM vs. FM or AFM). The higher energy and smaller lattice parameters of the NM structure can be connected to its inadequate Jahn-Teller (J-T) distortion represented by the ratio of the difference between the longest and shortest Mn-O distances to the average Mn-O distance. The optimized NM structure

11

shows only 5 to 6 % J-T distortion, whereas the magnetic structures show as much as 20 to 28 %, which is in good agreement with the 16 to 23 % that can be calculated based on the experimental data in Table 1.

Overall, our geometry-optimized fully-relaxed magnetic quenselite structures compared favorably with experimental results, although they have larger a and c lattice parameters than observed experimentally, a typical trend in DFT/GGA studies of layer type Mn oxides, such as $LiMnO_2$ and $ZnMn_3O_7 \cdot 3H_2O$ (Mishra and Ceder, 1999; Kwon et al., 2009). Full relaxation led to interatomic distances too large on average by 2 to 3 %, whereas constrained geometry optimization of the AFM structure, with lattice parameters and angles fixed at their experimental values while the internal coordinates of all ions were relaxed, showed excellent agreement with experiment, with interatomic distances that differed from experiment on average by << 1 % (fifth and sixth columns in Table 1).

Asymmetry in the interatomic distances for the Pb(II)-O pair in quenselite and in Pb(II) oxides is usually explained in terms of a stereoactive lone pair of $6s^2$ electrons (Bargar et al., 1997; Manceau et al., 2002), a result of hybridization between Pb-6s and Pb-6p atomic orbitals (Orgel, 1959). However, recent soft X-ray emission spectroscopy and DFT studies for a highly asymmetric α-PbO structure showed that the 6s states of Pb(II) in fact significantly hybridize with O-2p states. Specifically, the Pb-6s and O-2p states in α-PbO hybridize well below the Fermi energy (at about − 9 eV) and their filled antibonding states near the Fermi energy further mix with empty Pb-6p states (the mixing is mainly between O-2p and Pb-6p states), leading to the observed structural distortion (Walsh and Watson, 2005; Payne et al., 2006). Similar to α-PbO, our calculated density of states (DOS) for quenselite shows that the Pb-6s states (Fig. 4a)

mainly overlap with O-2p states deep in the valence band at about 9 eV below the Fermi energy (Fig. 4b and 4c) and the Pb-6p states mix mainly with O-2p states around $-$ 6 to $-$ 3 eV in the valence band. Additional insights from DFT analysis are revealed in Fig. 4b, where the peaks in the partial DOS for O$_H$ at about $-$ 7 eV correspond to bonding with H, and in Fig. 4c, where the spin-up states of O$_{3Mn}$ between $-$ 2 to 0 eV are spin-polarized states of O induced by the Mn(III) ions in quenselite.

3.2. Model birnessite nanoparticles

In the geometry-optimized nanodisks, the Mn-O distances in Mn octahedra [d(Mn-O)] fell into the 1.8 $-$ 2.0 Å range, with some variation at the lateral edges, where d(Mn-O) corresponding to terminal Mn-OH and Mn-OH$_2$ were 1.81 to 1.90 Å and 2.04 to 2.08 Å, respectively. The experimental average d(Mn-O) in hexagonal birnessite is about 1.90 Å (Galliot et al, 2003; Villalobos et al, 2006). The model nanodisks showed a slight relaxation of the Mn-Mn distance [d(Mn-Mn)] = 2.92 to 2.95 Å], while d(Mn-Mn) in our fully-periodic MnO$_2$ octahedral sheet was 2.90 Å [the corresponding experimental values are 2.87 to 2.88 Å, without noticeable relaxation for differing particle size (Galliot et al, 2003; Villalobos et al, 2006)]. The structural relaxation of nanodisks we observed can lead to a slight overestimation of the interatomic distances in Pb(II) surface complexes as compared to experiment. The distances along the O$_{III}$-O$_{III}$ edges of Mn(IV) octahedra were symmetric (approximately 2.8 Å), while the equivalent tridentate site in quenselite showed asymmetry, with O$_{III}$-O$_{III}$ distances of 2.9, 3.1, and 3.3 Å.

We determined the average Mn oxidation number in the model nanodisks by calculating the energy of the spin-up vs. spin-down states of Mn-3s (ΔE_{Mn_3s}) [see Kwon et al. (2008) for details], which corresponds experimentally to a splitting of the Mn-3s peak in X-ray photoemission spectra (Junta and Hochella, 1994; Galakhov et al., 2002). Experimental Mn-3s splitting data are not available for hexagonal birnessite, but a value is expected between those for γ-MnOOH and β-MnO$_2$ due to the presence of interlayer Mn(III). Although DFT generally underestimates the absolute experimental values of the splitting, mainly because of the lack of an excited-state treatment, a systematic trend in ΔE_{Mn_3s} with Mn oxidation number is preserved consistently with experiment (Fig. 5). We found calculated ΔE_{Mn_3s} values of 3.32 eV and 4.77 eV for the model birnessite nanodisk and quenselite, respectively, corresponding to Mn oxidation numbers of +IV and +III, as expected.

3.3. Interlayer surface complexes: Pb-TCS vs. Pb-TES

The geometry-optimized Pb-TCS structure showed good agreement with experiment (Table 2), differing from the latter by about 3 % (overestimation). Based on this agreement, our assumed octahedral coordination for Pb [i.e., binding with three mineral surface O and three H$_2$O (Fig. 1a)] is reasonable, particularly since the coordination number (CN) of adsorbed Pb [and even that of Pb(II) in aqueous solution] is challenging to determine directly by EXAFS analysis (Villalobos et al. 2005; Gourlaouen et al., 2006; Takahashi et al. 2007). The CN for d(Pb-Mn$_{1st}$), CN_{Mn}, obtained from EXAFS analysis is much smaller than crystallographic value of 6. Takahashi et al. (2007) interpreted this result as caused by variability of d(Pb-Mn$_{1st}$), as occurs in quenselite: they reported 4.09 Å (CN_{Mn} = 0.8) and 3.70 Å (CN_{Mn} = 1.0) of d(Pb-Mn$_{1st}$) based on

EXAFS spectra carefully analyzed in the wavenumber region $9 < k < 11$ Å^{-1}. Our DFT optimization of the TCS complex, however, predicted rather symmetric d(Pb-Mn$_{1st}$) ($CN_{Mn} = 6$), which agrees with most experimental results obtained from EXAFS spectra analyzed for wavenumbers up to $k < 10$ Å^{-1}.

In Pb-TES, we found that Pb is located very near the edge of the vacancy (i.e., the edge along O$_{II}$-O$_{II}$), away from the center of the tridentate cavity (Fig. 1b). Geometry optimization in fact moved the initial position of Pb from the center of the cavity toward a position near the O$_{II}$-O$_{II}$ edge. Flipping of the Pb(II) ion to form a bond with one of the remaining O$_{II}$ around the vacancy site, thus forming Pb-TCS, is preempted if a hydrating H$_2$O molecule is present which forms a strong H-bond with O$_{II}$. This effect implies that Pb(II) in an interlayer Pb-TES complex could move further into the vacancy site to form Pb-TCS depending on the local hydration environment. This possibility would make it difficult to detect Pb-TES and resolve its structural parameters using EXAFS spectroscopy.

We found that the TES site near a Mn(IV) vacancy is distorted (i.e., 2.7 Å for the O$_{II}$-O$_{III}$ distance and 3.1 Å for the O$_{II}$-O$_{II}$ distance). The Pb-O$_{III}$ distance ($CN = 1$) in Pb-TES was longer by 0.4 Å than the Pb-O$_{II}$ distance ($CN = 2$) and the nearest Pb-Mn distances were (each for $CN = 2$) 3.49 Å, 4.15 Å, and 4.75 Å. However, Lanson et al. (2002) estimated d(Pb-Mn$_{1st}$) to be only 3.02 Å based on XRD analysis. This disagreement with our results might stem from the composition of their birnessite (significant layer Mn^{3+} content), but the general agreement of the Pb-TCS distances between experiment and our DFT results suggests that such composition effects should be minor.

3.4. Surface complexes on nanoparticle edges: Pb-DES vs. Pb-DCS

Overall, Pb-DES surface complexes on the model birnessite nanoparticle edges tended to show larger Pb-O distances but smaller $Pb-Mn_{1st}$ distances than did the Pb-DCS complexes, with $d(Pb-Mn_{1st})$ then being characteristic for each complex (Table 3). Our DFT estimate of $d(Pb-Mn_{1st})$ in DES_0^H (O_I is protonated but O_{II} is not), 3.34 ± 0.05 Å, is in good agreement with experiment [3.23 to 3.25 Å at pH 5 to 7 (Takahashi et al., 2007)], given the expected minor overestimation of structural parameters (approximately 3 %, based on the geometry optimization of Pb-TCS). The larger $d(Pb-O)$ in DES_0^H than in Pb-TCS (2.49 vs. 2.41 Å) is also consistent with experiment, in that a slight reduction in average Pb-O distances was observed by Takahashi et al. (2007) in samples having a low estimated DES/TCS ratio. Evidently the major surface complex of Pb(II) occurring on birnessite nanoparticle edges should be DES, particularly the variant with O_I protonated (DES_0^H, Fig. 3).

We found that the protonation states of the surface O atoms to which Pb binds greatly affect surface complex structures. In Pb-DES, protonation of O_I significantly increased the $Pb-O_I$ distance, but decreased the $Pb-O_{II}$ distance by as much as 0.2 Å while also increasing the $Pb-Mn_{1st}$ and $Mn_{1st}-OPb$ distances (Table 3). In Pb-DCS, O_I protonation increased $Pb-Mn_{1st}$ and $Mn_{1st}-OPb$ distances by $0.2 - 0.3$ Å. Protonation of O_{II}, which is likely to occur at low pH [pznpc of birnessite < 4 (Murray, 1974)], prevented Pb(II) from binding with O_{II} at all; instead, Pb flips up onto the basal plane and binds to a proximate O_{III} (e.g., DES_H^0 in Fig. 3) and $d(Pb-Mn_{1st})$ significantly increases. In the case of DES_H^H, the $Pb-O_{III}$ distance (2.37 Å) became as small as the $Pb-O_I$ distance. According to bond valence concepts, O_{III}, being a saturated surface O, should be inert in respect to metal ion adsorption. In fact, binding with O_{III} does not occur for transition

16

metal ions (e.g., Ni^{2+}) and, therefore, its occurrence for Pb(II) must logically be attributed to the influence of $6s$ electrons. Our DFT analysis of electronic structure found that binding of Pb(II) with O_{III} indeed occurs mainly through interactions between O-$2p$ and Pb-$6s$ orbitals, just as occurs in quenselite (Fig. 4).

The stability of DES_0^H over DES_0^0 can be understood by examining bond valences and the DFT-calculated magnetic moments of O in addition to the insight offered by a total energy comparison. The total energy of DES_0^H was lower than DES_0^0 by 58 kJ/mol after a geometry optimization performed without hydrating H_2O molecules. According to Pauling's second rule, in DES_0^0, O_I receives 0.67 valence units (v.u.) each from Mn (i.e., 4/6) and Pb (i.e., 2/3) to make a total of 1.34 v.u., which is well below the 2.00 v.u. required for saturating O(-II). Although O_I in DES_0^0 is undersaturated, the protonated O_I in DES_0^H becomes saturated because H contributes about + 0.8 v.u., with and elongation of the Pb-O_I bond (2.30 Å for DES_0^0 vs. 2.49 Å for DES_0^H) compensating for any oversaturation induced by protonation. This conclusion is supported by our calculated spin magnetic moments of O based on a population analysis of projected planewave states. The magnetic moment of O in a H_2O molecule is calculated to be 0.00 μ_B. The calculated magnetic moments of the terminal O in $\equiv$Mn-O_IH, $\equiv$Mn-O_IH$_2$, and $\equiv$Mn$_2$-O_{II}H are equal to about + 0.10 μ_B, 0.00 μ_B, and $-$ 0.04 to $-$ 0.06 μ_B, respectively. The magnetic moment of O_{III} is calculated to be $-$ 0.04 to $-$ 0.06 μ_B, a typical consequence of O-$2p$–Mn-$3d$ hybridization (Kanamori and Terakura, 2001). Thus the magnetic moment of O indicates the degree of undersaturation of an O ion, with undersaturated O having a positive moment and saturated O having no magnetic moment or a slightly negative moment. When O_I in DES is protonated (DES_0^0 vs. DES_0^H), we found that the magnetic moment drops from + 0.16 μ_B to 0.00 μ_B,

17

indicating that $O_{I\,has}$ become saturated upon protonation. This same drop was found in Pb-DCS as well, implying DCS_0^H would be a stable Pb(II) surface species, if it existed.

The experimentally-observed preference of Pb-DES over Pb-DCS (Takahashi, 2007) can be explored further by a total-energy comparison between the two surface complexes based on DFT geometry optimization performed without hydrating H_2O. Without these water molecules, we found that, during geometry optimization with Pb initially placed at its position in Pb-DCS, the metal ion always flips downward to bind with O_{II} when O_{II} is deprotonated, but upward to bind with O_{III} when O_{II} is protonated (See supporting information, EA-2). Thus unhydrated Pb-DCS itself cannot be geometry-optimized, but the total energy of DES was lower than that of the initial DCS configuration after geometry optimization by more than 43 kJ/mol. These insights, which extend what EXAFS spectroscopy alone can provide, suggest that the complex has two potential energy minima, one with Pb positioned near O_{II} and one with it positioned near O_{III}, with positions of Pb at locations between O_{II} and O_{III} (i.e., DCS) corresponding to an unstable maximum. Hydrating H_2O could develop local minima of Pb around O_I (Fig. 3), however, implying that Pb-DCS may actually occur, depending on local hydration conditions, while the major edge-surface species still would be Pb-DES.

Besides these causes, structural similarity among competing complexes could also underlie the non-detection of Pb-DCS in EXAFS spectral analyses. The protonated Pb-DCS complex, DCS_0^H, has interatomic distances that are very similar to those in Pb-TCS (Tables 2 and 3). A similarity in structural parameters is also found between Pb-TES near a Mn vacancy and the protonated Pb-DES complexes, in that the Pb-DES complexes with protonated O_{II} have a d(Pb-Mn$_{1st}$) value very close to that in Pb-TES (Tables 2 and 3). These similarities may be

involved with the reported difficulties in detecting edge-surface species (e.g., DES_H^0) on well-crystallized birnessite at pH 4 (Takahashi et al., 2007) and in resolving the structural parameters of Pb-TES from EXAFS spectral analysis (Manceau et al., 2002).

REFERENCES

Banerjee D. and Nesbitt H. W. (1999) Oxidation of aqueous Cr(III) at birnessite surfaces: Constraints on reaction mechanism. *Geochim. Cosmochim. Acta* **63**, 1671-1687.

Bargar J. R., Brown G. E., and Parks G. A. (1997) Surface complexation of Pb(II) at oxide-water interfaces: I. XAFS and bond-valence determination of mononuclear and polynuclear Pb(II) sorption products on aluminum oxides. *Geochim. Cosmochim. Acta* **61**, 2617-2637.

Barnard A. S. (2009) How can ab initio simulations address risks in nanotech? *Nat. Nanotechnol.* **4**, 332-335.

Beak D. G., Basta N. T., Scheckel K. G., and Traina S. J. (2008) Linking solid phase speciation of Pb sequestered to birnessite to oral Pb bioaccessibility: Implications for soil remediation. *Environ. Sci. Technol.* **42**, 779-785.

Boonfueng T., Axe L., Xu Y., and Tyson T. A. (2006) Nickel and lead sequestration in manganese oxide-coated montmorillonite. *J. Colloid Interface Sci.* **303**, 87-98.

Clark S. J., Segall M. D., Pickard C. J., Hasnip P. J., Probert M. J., Refson K., and Payne M. C. (2005) First principles methods using CASTEP. *Z. Kristallogr.* **220**, 567-570.

Dong D. M., Derry L. A., and Lion L. W. (2003) Pb scavenging from a freshwater lake by Mn oxides in heterogeneous surface coating materials. *Water Res.* **37**, 1662-1666.

Drits V. A., Lanson B., Bougerol-Chaillout C., Gorshkov A. I., and Manceau A. (2002) Structure of heavy-metal sorbed birnessite: Part 2. Results from electron diffraction. *Am. Mineral.* **87**, 1646-1661.

Gaillot A. C., Flot D., Drits V. A., Manceau A., Burghammer M., and Lanson B. (2003) Structure of synthetic K-rich birnessite obtained by high-temperature decomposition of $KMnO_4$. I. Two-layer polytype from 800 °C experiment. *Chem. Mater.* **15**, 4666-4678.

Galakhov V. R., Demeter M., Bartkowski S., Neumann M., Ovechkina N. A., Kurmaev E. Z., Lobachevskaya N. I., Mukovskii Y. M., Mitchell J., and Ederer D. L. (2002) Mn 3s exchange splitting in mixed-valence manganites. *Phys. Rev. B* **65**, 113102.

Gourlaouen C., Gerard H., and Parisel O. (2006) Exploring the hydration of Pb^{2+}: Ab initio studies and first-principles molecular dynamics. *Chem. Eur. J.* **12**, 5024-5032.

Grangeon S., Lanson B., Lanson M., and Manceau A. (2008) Crystal structure of Ni-sorbed synthetic vernadite: a powder X-ray diffraction study. *Mineral. Mag.* **72**, 1279-1291.

Hattori T., Saito T., Ishida K., Scheinost A. C., Tsuneda T., Nagasaki S., and Tanaka S. (2009) The structure of monomeric and dimeric uranyl adsorption complexes on gibbsite: A combined DFT and EXAFS study. *Geochim. Cosmochim. Acta* **73**, 5975-5988.

Hochella M. F., Moore J. N., Putnis C. V., Putnis A., Kasama T., and Eberl D. D. (2005) Direct observation of heavy metal-mineral association from the Clark Fork River Superfund Complex: Implications for metal transport and bioavailability. *Geochim. Cosmochim. Acta* **69**, 1651-1663.

Junta J. and Hochella M. F. (1994) Manganese(II) oxidation at mineral surfaces - a microscopic and spectroscopic study. *Geochim. Cosmochim. Acta* **58**, 4985-4999.

Kanamori J. and Terakura I. (2001) A general mechanism underlying ferromagnetism in transition metal compounds. *J. Phys. Soc. Jpn.* **70**, 1433-1434.

Kwon, K.D., Refson, K., Sposito, G. (2008) Defect-induced photoconductivity in layered manganese oxides: A density functional theory study. *Phys. Rev. Lett.* **100**, 146601.

Kwon K. D., Refson K., and Sposito G. (2009) Zinc surface complexes on birnessite: A density functional theory study. *Geochim. Cosmochim. Acta* **73**, 1273-1284.

Lanson B., Drits V. A., Gaillot A. C., Silvester E., Plancon A., and Manceau A. (2002) Structure of heavy-metal sorbed birnessite: Part 1. Results from X-ray diffraction. *Am. Mineral.* **87**, 1631-1645.

Lanson B., Marcus M. A., Fakra S., Panfili F., Geoffroy N., and Manceau A. (2008) Formation of Zn-Ca phyllomanganate nanoparticles in grass roots. *Geochim. Cosmochim. Acta* **72**, 2478-2490.

Manceau A., Lanson B., and Drits V. A. (2002) Structure of heavy metal sorbed birnessite. Part III: Results from powder and polarized extended X-ray absorption fine structure spectroscopy. *Geochim. Cosmochim. Acta* **66**, 2639-2663.

Marzari N. (2006) Realistic modeling of nanostructures using density functional theory. *MRS Bulletin* **31**, 681-687.

Mason S. E., Iceman C. R., Tanwar K. S., Trainor T. P., and Chaka A. M. (2009) Pb(II) Adsorption on isostructural hydrated alumina and hematite (0001) surfaces: A DFT study. *J. Phys. Chem. C* **113**, 2159-2170.

Matocha C. J., Elzinga E. J., and Sparks D. L. (2001) Reactivity of Pb(II) at the Mn(III,IV) (oxyhydr)oxide-water interface. *Environ. Sci. Technol.* **35**, 2967-2972.

Mishra S. K. and Ceder G. (1999) Structural stability of lithium manganese oxides. *Phys. Rev. B* **59**, 6120-6130.

Monkhorst H. J. and Pack J. D. (1976) Special points for Brillouin-zone integrations. *Phys. Rev. B* **13**, 5188-5192.

Morin G., Juillot F., Ildefonse P., Calas G., Samama J. C., Chevallier P., and Brown G. E. (2001) Mineralogy of lead in a soil developed on a Pb-mineralized sandstone (Largentiere, France). *Am. Mineral.* **86**, 92-104.

Murray J. W. (1974) The surface chemistry of hydrous manganese dioxide. *J. Colloid Interface Sci.* **46**, 357-371.

Orgel L. E. (1959) The stereochemistry of B subgroup metals. Part II. The inert pair. *J. Chem. Soc.* **4**, 3815-3819.

Pask J. E., Singh D. J., Mazin I. I., Hellberg C. S., and Kortus J. (2001) Structural, electronic, and magnetic properties of MnO. *Phys. Rev. B* **64**, 024403.

Payne D. J., Egdell R. G., Walsh A., Watson G. W., Guo J., Glans P. A., Learmonth T., and Smith K. E. (2006) Electronic origins of structural distortions in post-transition metal oxides: Experimental and theoretical evidence for a revision of the lone pair model. *Phys. Rev. Lett.* **96**, 157403.

Payne M. C., Teter M. P., Allan D. C., Arias T. A., and Joannopoulos J. D. (1992) Iterative minimization techniques for *ab initio* total-energy calculations: molecular-dynamics and conjugate gradients. *Rev. Mod. Phys.* **64**, 1045-1097.

Perdew J. P., Burke K., and Ernzerhof M. (1996) Generalized gradient approximation made simple. *Phys. Rev. Lett.* **77**, 3865-3868.

Pfrommer B. G., Cote M., Louie S. G., and Cohen M. L. (1997) Relaxation of crystals with the quasi-Newton method. *J. Comput. Phys.* **131**, 233-240.

Rouse R. C. (1971) Crystal structure of quenselite. *Z. Kristallogr.* **134**, 321-332.

Saratovsky I., Wightman P. G., Pastén P. A., Gaillard J. F., and Poeppelmeier K. R. (2006) Manganese oxides: Parallels between abiotic and biotic structures. *J. Am. Chem. Soc.* **128**, 11188-11198.

Sherman D. M., Peacock C. L., and Hubbard C. G. (2008) Surface complexation of U(VI) on goethite (α-FeOOH). *Geochim. Cosmochim. Acta* **72**, 298-310.

Singh D. J. (1997) Magnetic and electronic properties of $LiMnO_2$. *Phys. Rev. B* **55**, 309-312.

Takahashi Y., Manceau A., Geoffroy N., Marcus M. A., and Usui A. (2007) Chemical and structural control of the partitioning of Co, Ce, and Pb in marine ferromanganese oxides. *Geochim. Cosmochim. Acta* **71**, 984-1008.

Tebo B. M., Bargar J. R., Clement B. G., Dick G. J., Murray K. J., Parker D., Verity R., and Webb S. M. (2004) Biogenic manganese oxides: Properties and mechanisms of formation. *Annu. Rev. Earth Planet. Sc.* **32**, 287-328.

Vanderbilt D. (1990) Soft self-consistent pseudopotentials in a generalized eigenvalue formalism. *Phys. Rev. B* **41**, 7892-7895.

Villalobos M., Bargar J., and Sposito G. (2005) Mechanisms of Pb(II) sorption on a biogenic manganese oxide. *Environ. Sci. Technol.* **39**, 569-576.

Villalobos M., Lanson B., Manceau A., Toner B., and Sposito G. (2006) Structural model for the biogenic Mn oxide produced by *Pseudomonas putida*. *Am. Mineral.* **91**, 489-502.

Villalobos M., Toner B., Bargar J., and Sposito G. (2003) Characterization of the manganese oxide produced by *Pseudomonas putida* strain MnB1. *Geochim. Cosmochim. Acta* **67**, 2649-2662.

Walsh A. and Watson G. W. (2005) The origin of the stereochemically active Pb(II) lone pair: DFT calculations on PbO and PbS. *J. Solid State Chem.* **178**, 1422-1428.

Wilson A. R., Lion L. W., Nelson Y. M., Shuler M. L., and Ghiorse W. C. (2001) The effects of pH and surface composition of Pb adsorption to natural freshwater biofilms. *Environ. Sci. Technol.* **35**, 3182-3189.

Xu Y., Boonfueng T., Axe L., Maeng S., and Tyson T. (2006) Surface complexation of Pb(II) on amorphous iron oxide and manganese oxide: Spectroscopic and time studies. *J. Colloid Interface Sci.* **299**, 28-40.

Zhang Z., Fenter P., Kelly S. D., Catalano J. G., Bandura A. V., Kubicki J. D., Sofo J. O., Wesolowski D. J., Machesky M. L., Sturchio N. C., and Bedzyk M. J. (2006) Structure of hydrated Zn^{2+} at the rutile TiO_2 (110)-aqueous solution interface: Comparison of X-ray standing wave, X-ray absorption spectroscopy, and density functional theory results. *Geochim. Cosmochim. Acta* **70**, 4039-4056.

Figure 1. Geometry-optimized surface complexes of Pb(II) on a Mn(IV) vacancy in a model hexagonal birnessite nanoparticle: a triple corner-sharing (TCS) complex; a triple edge-sharing (TES) complex. (a) TCS and TES complexes positioned above and below a Mn(IV) vacancy. (b) View of TES perpendicular to the *a-b* plane (terminal O and H are omitted for visual clarity) with TCS below the vacancy. Dotted lines show coordination with H_2O. Color scheme: red = O; gray = Pb; white = H; purple = Mn.
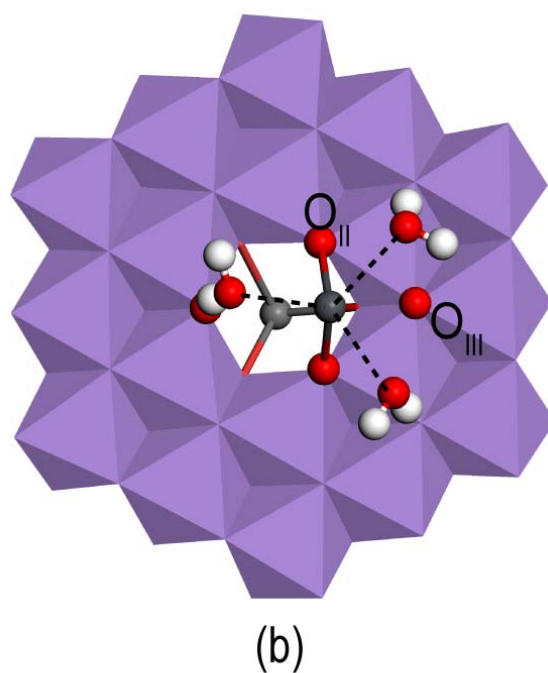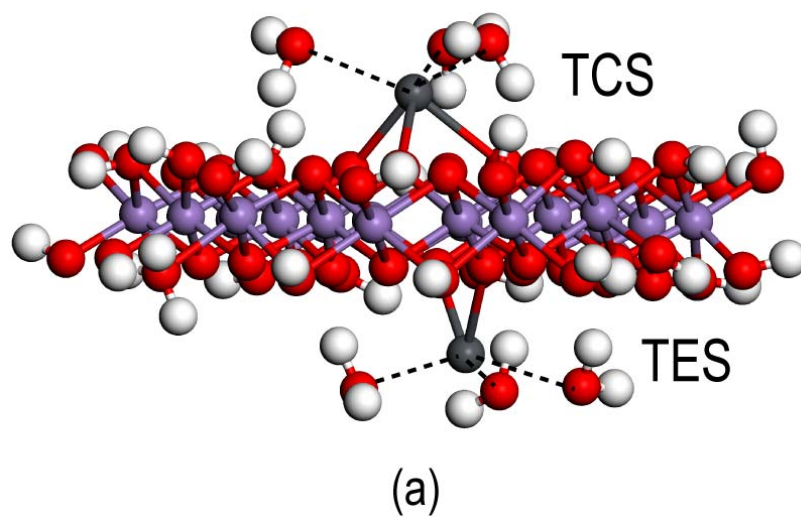

(a)

(b)

Figure 2. Geometry-optimized quenselite (PbMnO$_2$OH) projected onto (a) the *b-c* plane and (b) the *a-c* plane. Double-headed arrows delineate interlayer Pb(II) distances (Å) from surface O. Color scheme: gray = Pb, red = O, white = H.
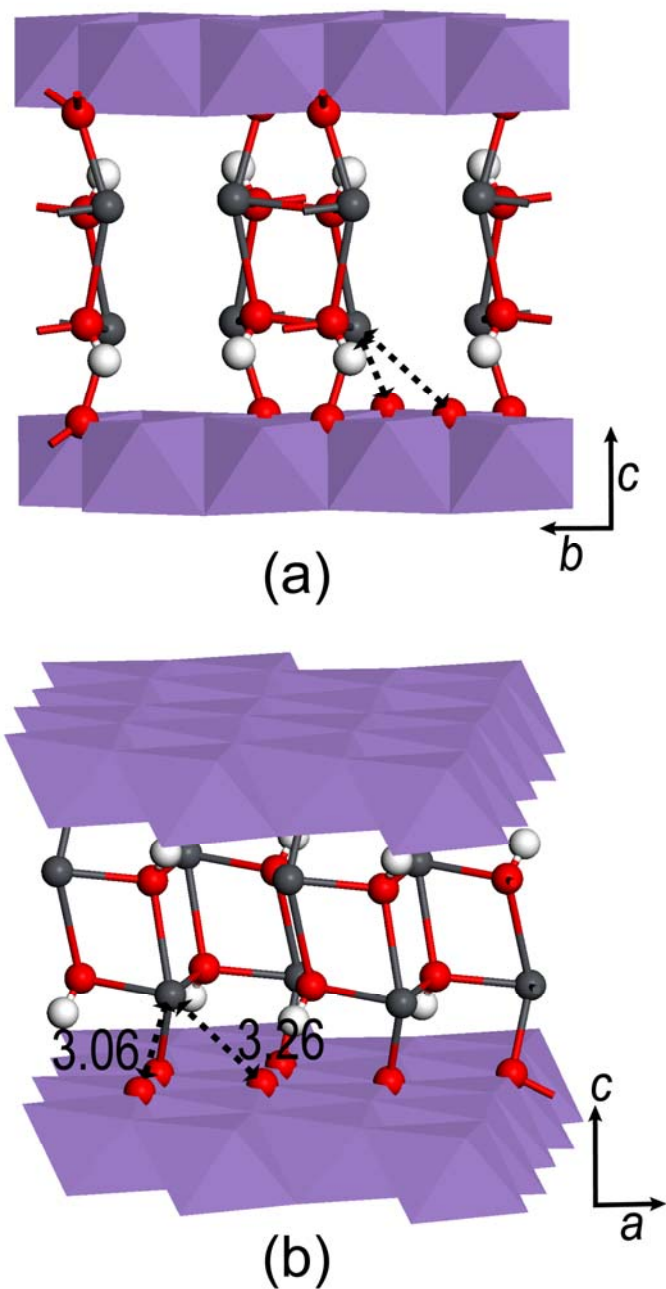
Figure 3. Geometry-optimized surface complexes of Pb(II) at the lateral edge of a model birnessite nanoparticle. The superscripts and subscripts on DES (double edge-sharing complex) and DCS (double corner-sharing complex) represent the protonation state of O_I and O_{II}, which are bonded to one Mn and two Mn, respectively. Color scheme: red = O; gray = Pb; white = H. Terminal O and H are omitted for visual clarity.
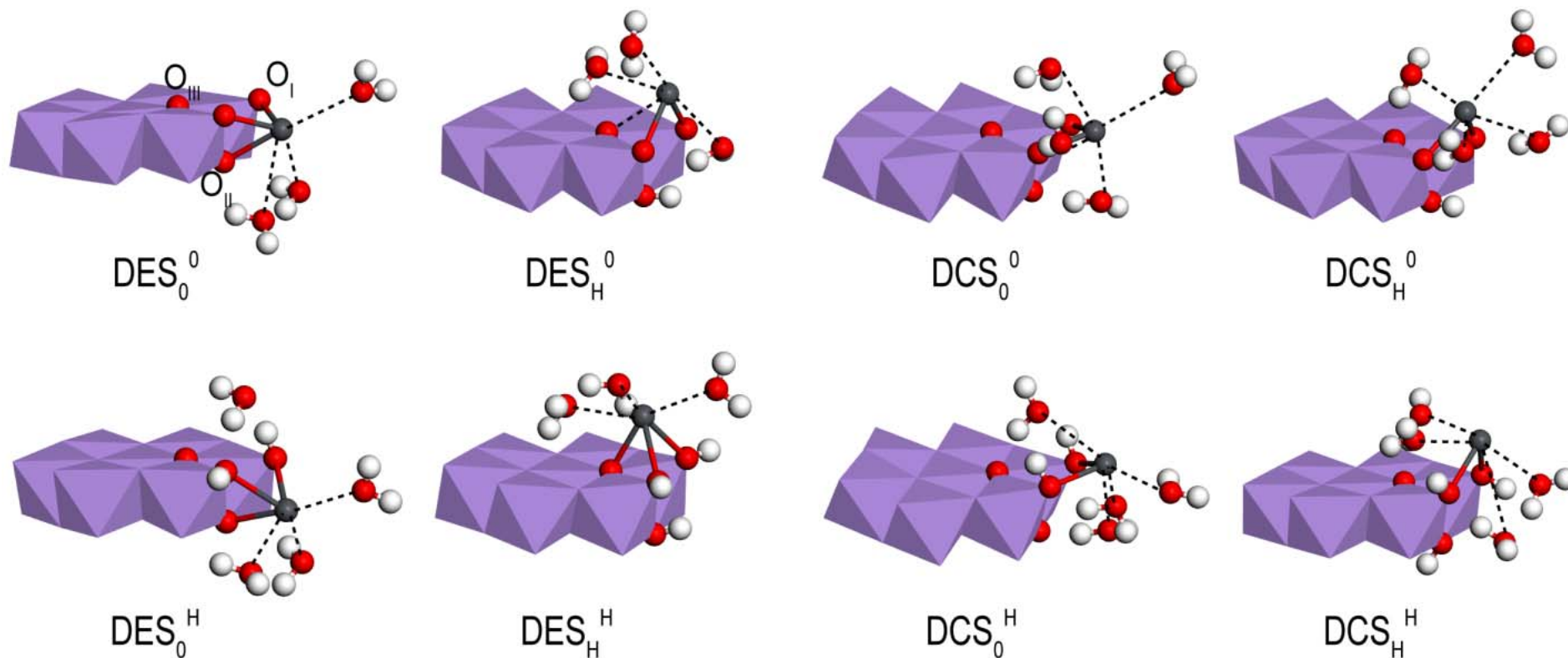
Figure 4. Partial density of states (DOS) in quenselite, showing the contribution of: (a) Pb, (b) O bonded to H (O_H), and (c) surface O (O_{3Mn}) which coordinate with interlayer Pb. The dotted line represents the Fermi energy (E_F) and arrows show the spin-up and spin-down contribution of DOS. The Gaussian smearing width of the DOS was 0.05 eV. The semiconducting band gap for quenselite was calculated to be 0.55 eV in DFT.
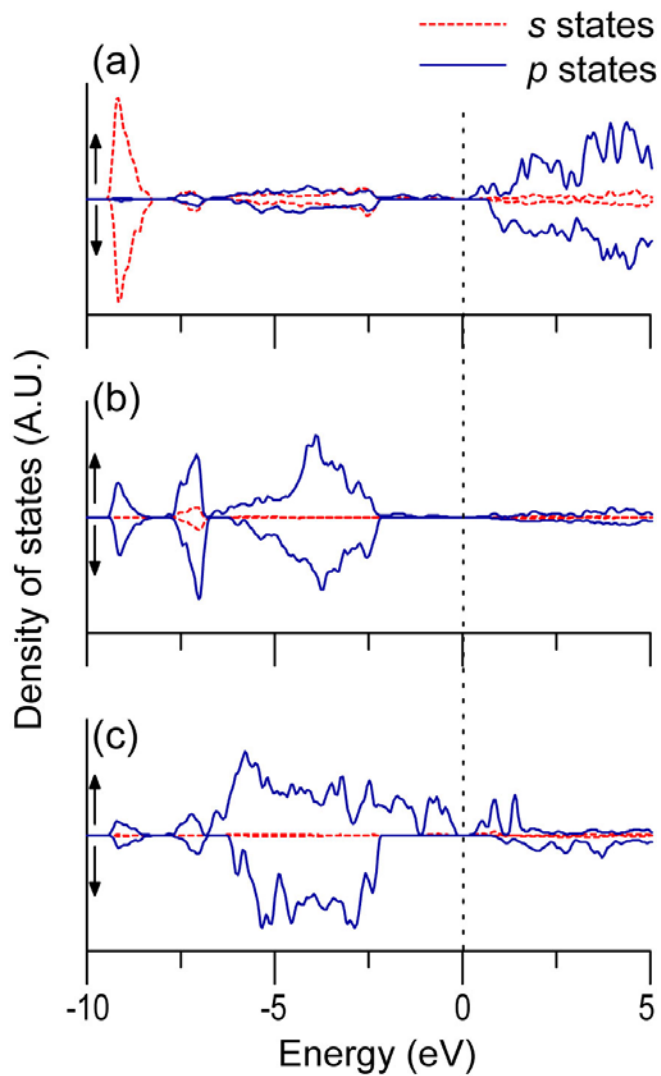
Figure 5. Multiplet splitting of Mn-3*s* plotted against Mn oxidation number for geometry-optimized MnO, quenselite, and a model birnessite nanodisk. The experimental XPS data are for MnCO$_3$, γ-MnOOH, and β-MnO$_2$ (Junta and Hochella, 1994) and MnO, LiMnO$_2$, and Li$_2$MnO$_3$ (Galakhov et al., 2002).
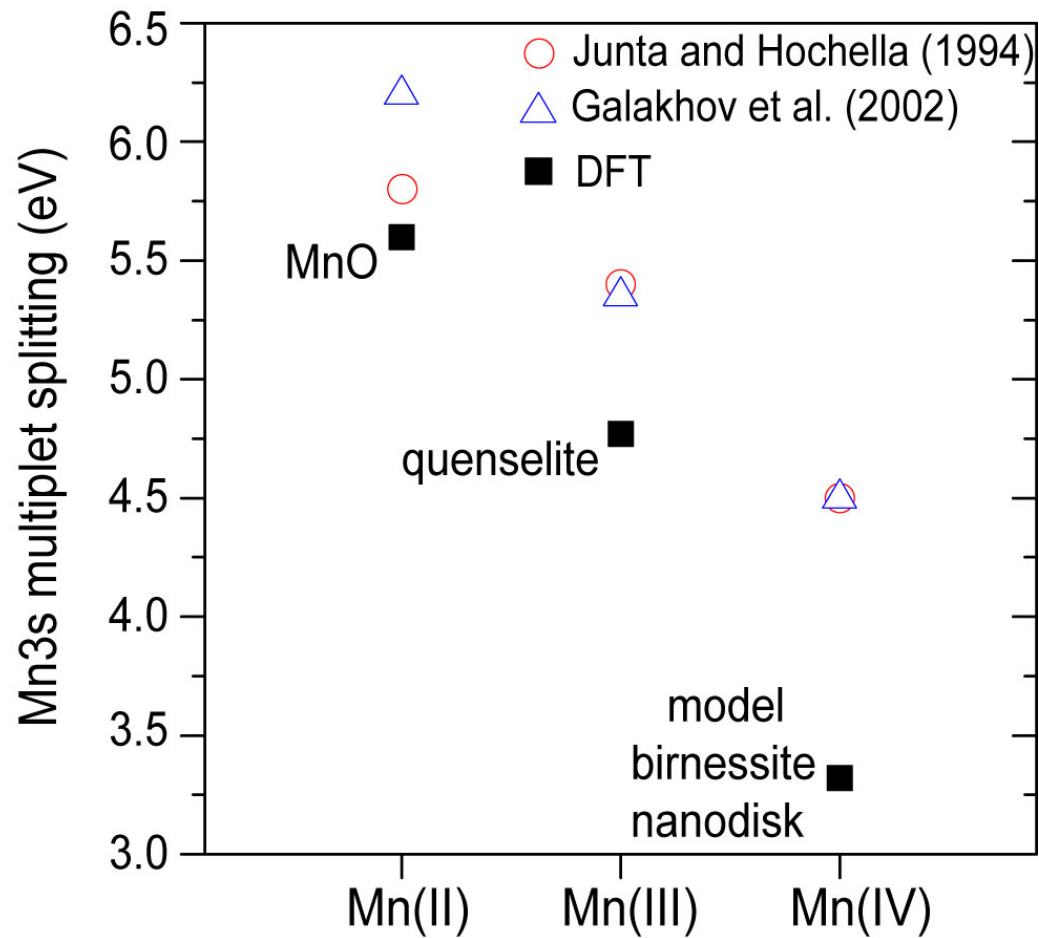
Table 1. Total energy per formula unit (1 eV= 96.483 kJ/mol, expressed relative to FM ordering) and structural parameters (Å) of quenselite (PbMnO$_2$OH) geometry-optimized without (NM) and with spin polarization (FM, ferromagnetic; AFM, antiferromagnetic ordering).

| | | DFT | | | Experiment |
	NM	FM	AFM	AFM_fixed[a]	XRD[b]
E (eV)	+1.05	0	-0.1	-0.07	
a	5.30	5.81	5.80	5.61	5.61
b	5.54	5.76	5.72	5.70	5.70
c	9.48	9.40	9.41	9.15	9.15
Pb-O$_H$	2.35	2.38	2.37	2.38	2.31
	2.37	2.40	2.39	2.39	2.36
	3.00	2.89	2.90	2.74	2.76
Pb-O$_{layer}$	2.33	2.28	2.28	2.29	2.22
	2.90	3.05	3.04	3.00	2.99
	3.15	3.25	3.24	3.12	3.16
Pb-Mn	3.45	3.47	3.47	3.46	3.43
	3.49	3.68	3.68	3.59	3.58
	3.90	3.99	3.99	4.00	3.96
Mn-O	2.02	1.93	1.93	1.92	1.93
	1.93	1.96	1.95	1.95	1.98
	2.01	2.34	2.35	2.27	2.25
	1.90	1.92	1.91	1.93	1.90
	1.98	1.94	1.94	1.92	1.95
	2.03	2.50	2.51	2.39	2.37
Mn-Mn	2.43	2.82	2.78	2.78	2.78
	3.09	2.94	2.94	2.92	2.93
Pb-Pb	3.82	4.00	4.02	4.00	3.97

The unit cell angles (°), α, β, γ, for NM, FM (or AFM, and the experimentally-determined structures are 90.0, 90.8, 90.0; 90.0, 93.4, 90.0; and 90.0, 93.0, 90.0, respectively.
[a]Internal coordinates of all ions were relaxed with the lattice parameters fixed at experimental values.
[b]Rouse (1971).

Table 2. Interatomic distances (Å, mean plus standard deviation) in geometry-optimized TCS and TES surface complexes of Pb(II) (See Fig. 1).

Atom pair	DFT geometry optimization		Experimental values	
	TCS	TES	TCS	TES
Pb-O_{II}	2.41 ($\pm$ 0.06)	2.39 ($\pm$ 0.07)[a]	2.29 - 2.34[b] 2.31 $\pm$ 0.02[c]	2.25[d]
Pb-OH_2	2.79 ($\pm$ 0.08)	2.70 ($\pm$ 0.07)		2.60[d]
Pb-Mn_{1st}	3.84 ($\pm$ 0.04)	3.49 ($\pm$ 0.04)[a]	3.73 - 3.76[b] 3.74, 3.81[c]	3.02[d]

[a] The coordination number is 2. The d(Pb-O_{III}) = 2.81 Å and d(Pb-Mn_{2nd}) = 4.15 Å.

[b] EXAFS analysis with the Debye-Waller factor, σ^2, = 0.008 Å^2 and the effective coordination number (CN) for d(Pb-Mn_{1st}), CN_{Mn}, = 0.5 to 1.0 (Takahashi et al., 2007).

[c] EXAFS analysis with σ = 0.07 (CN_{Mn} = 2) and 0.09 Å (CN_{Mn} = 0.5) for Pb on Na-birnessite and vernadite, respectively (Morin et al., 2001).

[d] XRD pattern analysis (sample PbBi 58) of Lanson et al. (2002) with profile-weighted R factor, R_{wp} = 0.2 %. The d(Pb-Mn_{1st}) value for TCS was 3.81 Å (3.78 Å in EXAFS). In EXAFS, the Pb-TES complex was detected but interatomic distances were not resolvable (Manceau et al., 2002).
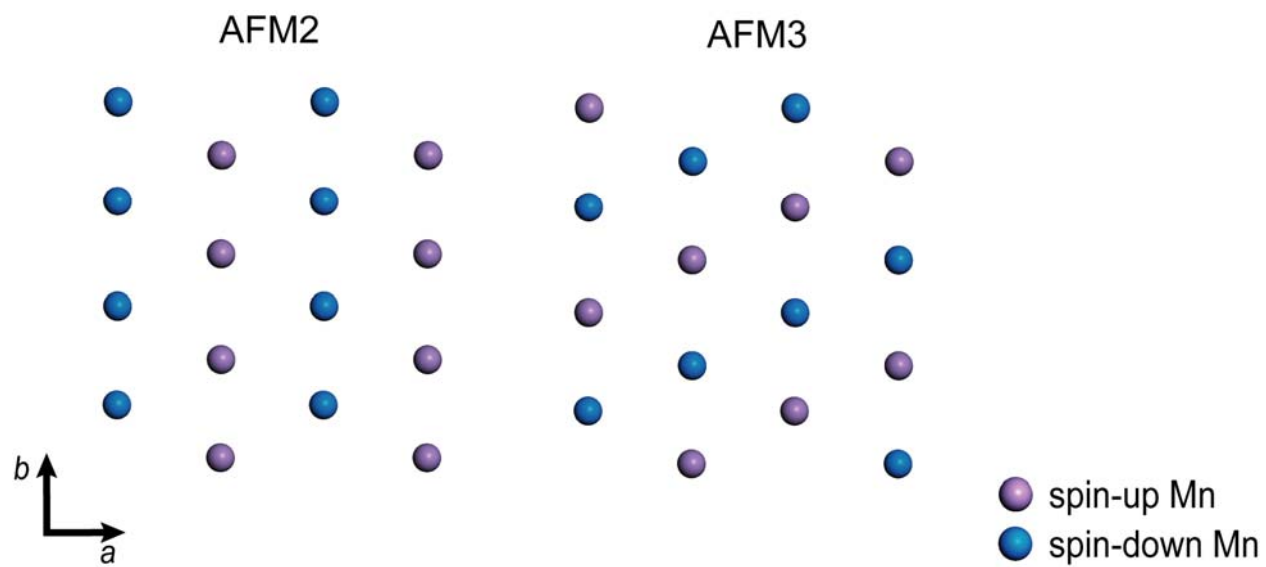
Table 3. Interatomic distances (Å) of geometry-optimized Pb-DES and Pb-DCS structures[a].

Atom pair	Pb-DES				Pb-DCS			
	DES_0^O	DES_0^H	DES_H^O	DES_H^H	DCS_0^O	DCS_0^H	DCS_H^O	DCS_H^H
Pb-O_I	2.30 (± 0.03)	2.49 (± 0.05)	2.29	2.53 (± 0.03)	2.28	2.32 (± 0.03)	2.28	2.33 (± 0.06)
Pb-O_{II}	2.53 (± 0.03)	2.36 (± 0.02)			3.38 (± 0.02)	3.53 (± 0.02)		
Pb-O_{III}			2.99 (± 0.04)	2.37			3.44	3.46
Pb-OH_2	3.06 (± 0.51)	2.71(± 0.28)	2.79 (± 0.15)	2.71 (± 0.17)	3.03 (± 0.46)	2.81 (± 0.32)	2.90 (± 0.25)	2.73 (± 0.31)
Pb-Mn_{1st}	3.23	3.34 (± 0.05)	3.46 (± 0.02)	3.45 (± 0.05)	3.55 (± 0.02)	3.82 (± 0.04)	3.62	3.89 (± 0.04)
Mn_{1st}-OPb	1.75	1.94 (± 0.03)	1.77	1.94	1.76	2.01 (± 0.02)	1.77	2.03 (± 0.04)

[a]Interatomic distances for each complex are averages of results for two or three geometry-optimized structures with different initial configurations involving the H_2O positions. Standard deviations are reported in parentheses or are < 0.02 Å. Superscripts and subscripts on DES and DCS indicate the protonation state of O_I and O_{II}, respectively (e.g., DES_H^O means O_I is not protonated while O_{II} is protonated; Fig. 3).
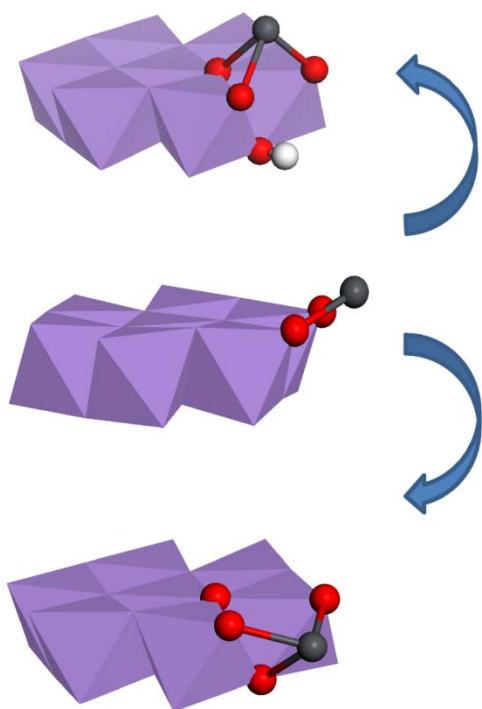
EA-1. Antiferromagnetic variants (AFM2 and AFM3) examined for the Mn(III) octahedral sheet in quenselite.

EA-2. Interatomic distances in geometry-optimized Pb-DCS without hydrating H_2O. The initial configuration of Pb, the DCS complex (center), was unstable relative to Pb-DES, with Pb finally bonding to either O_{II} (bottom) or O_{III} (top) depending on the protonation state of O_{II}. A stable Pb-DCS was not found under geometry optimization without introducing hydrating H_2O.

Atom pair	Distance (Å)	
	DES_0^{0w}	DES_H^{0w}
Pb-O_I	2.22	2.21
Pb-O_{II} or -O_{III}	2.39	2.47*
Pb-Mn_{1st}	3.13	3.17
Mn_{1st}-OPb	1.76	1.77

*Pb-O_{III} distances.